



Universidad Autónoma  
de Santo Domingo

# SIMULATION OF THE ELECTROMAGNETIC FIELD INSIDE THE ALPHA-G ANTIHYDROGEN TRAP

José Rojas    Supervisor: Dr. Adam Powell

*Instituto de Física, Universidad Autónoma de Santo Domingo, Alma Mater, Santo Domingo 10105,  
Dominican Republic*

*CERN, Esplanade des Particules 1, 1211 Geneva 23, Switzerland.*

August, 2025

## Abstract

The apparent scarcity of antimatter—the counterpart to matter—represents one of the most profound mysteries in modern physics. Theoretical considerations suggest that equal amounts of matter and antimatter were produced in the early universe, and the fundamental laws of physics make no intrinsic distinction between the two. Nevertheless, the observable universe appears to be overwhelmingly composed of ordinary matter, a phenomenon that has motivated extensive research worldwide, particularly at leading facilities such as CERN (the European Organization for Nuclear Research).

A prominent effort in this area is the ALPHA Experiment at CERN, which has achieved significant progress in the trapping, cooling, and microwave spectroscopy of antihydrogen. Central to these studies is the Alpha-g apparatus, a vertical magnetic trap for antimatter that enables high-precision experiments, including microwave spectroscopy of antihydrogen atoms and investigations of gravitational effects on antimatter. The complex geometries of the Penning traps within the Alpha-g apparatus make it extremely challenging to develop an exact analytical model of the electromagnetic fields following the injection of microwave signals. This project attempts to address this challenge by developing a computational simulation of the electromagnetic fields within the antihydrogen trap, providing a foundation for more precise studies.

# 1 Acknowledgments

I am extremely fortunate to have been involved with the ALPHA antihydrogen experiment at CERN in Geneva, Switzerland during a particularly exciting time. Thanks to exceptional scientists in the ALPHA collaboration with whom I had the opportunity to work and learn from. I would particularly like to express my gratitude to my Supervisor Dr. Adam Powell for all the support provided during this project and to Sean Garret for all the helpful discussions. I would also like to thank the Doctors Melvin Arias and Vladimir Pérez in the Dominican Republic, since without their support this would not have been possible.

# Contents

<b>1</b>	<b>Acknowledgments</b>	<b>1</b>
<b>2</b>	<b>Background Information</b>	<b>2</b>
2.1	Antimatter . . . . .	2
2.2	Antihydrogen formation and trapping . . . . .	3
2.3	Antimatter Experiments and Alpha . . . . .	3
2.4	Applications of Microwave Injection . . . . .	3
2.4.1	Microwave Spectroscopy . . . . .	3
2.4.2	ECR Magnetometry . . . . .	4
<b>3</b>	<b>Alpha-g Hardware Overview</b>	<b>5</b>
<b>4</b>	<b>Simulations</b>	<b>10</b>
4.1	Software ANSYS HFSS . . . . .	10
4.2	Base Case 1 . . . . .	10
4.3	Base Case 2 . . . . .	14
4.4	Addition of a Microwave Absorbing Material . . . . .	18
4.5	Realistic Case . . . . .	20
<b>5</b>	<b>Conclusions</b>	<b>26</b>

## 2 Background Information

### 2.1 Antimatter

Most particles of matter have corresponding antiparticles with the same mass and spin but opposite values of certain quantum numbers, such as electric charge, baryon number, or lepton number. In some cases, however—such as the photon—the particle is its own antiparticle. The idea of antimatter emerged not from experiment but from theory, when Paul Dirac, in 1928, sought to construct a version of quantum mechanics consistent with special relativity. His efforts led to the formulation of the Dirac equation,

$$(i\gamma^\mu\partial_\mu - m)\psi(x) = 0, \tag{1}$$

where  $m$  is a parameter interpreted as mass and  $\gamma^\mu$  are the Gamma Matrices gave negative energy solutions and the physical interpretation of the equation became that all spin 1/2 particles must have a pair with an opposite charge, known as antimatter.

The first discovered antimatter particle was the positron, identified by Carl David Anderson in 1932 through a cloud chamber experiment, in which a particle with the same properties as the electron was observed but curved in the opposite direction under a magnetic field, indicating an opposite electric charge [2]. Since then, antiparticle counterparts have been discovered for nearly all fundamental particles.

The experimental confirmation of antimatter validated Dirac's theoretical framework and firmly established the concept as a physical reality. However, it also raised new questions in cosmology. Standard models of the Big Bang predict that matter and antimatter should have been created in equal amounts in the early universe. Yet, astronomical observations reveal a cosmos overwhelmingly dominated by matter, with almost no primordial antimatter present. This striking imbalance, known as the baryon asymmetry problem, remains one of the deepest unresolved challenges in modern physics and continues to motivate research at the intersection of particle physics and cosmology.

## 2.2 Antihydrogen formation and trapping

The production of antihydrogen in the ALPHA experiment is achieved by carefully merging confined plasmas of antiprotons and positrons. This is accomplished through controlled manipulations of their respective electrostatic confinement potentials. Among the various mechanisms proposed for antihydrogen formation, the dominant process is believed to be three-body recombination. In this scenario, two positrons interact in the presence of an antiproton; one of the positrons loses sufficient energy to bind with the antiproton and form antihydrogen, while the second positron carries away the excess energy:

$$e^+ + e^+ + \bar{p} \rightarrow \bar{H} + e^+. \quad (2)$$

To enhance the production rate, several other advanced techniques for antihydrogen synthesis are being developed and applied in parallel experiments. A comprehensive discussion of these approaches can be found in [3]. Once antihydrogen is formed, the challenge shifts to confinement. Unlike charged particles, which can be effectively stored in Penning traps, antihydrogen is electrically neutral and thus requires a different method of trapping. The solution relies on its magnetic properties. As a diamagnetic atom with a nonzero magnetic moment, antihydrogen can be confined in a magnetic minimum trap—commonly referred to as an Ioffe–Pritchard trap, or “magnetic bottle.” In such a configuration, the trappable states of the atom are confined by the spin dependent potential:

$$U = -\vec{\mu} \cdot \vec{B}. \quad (6)$$

## 2.3 Antimatter Experiments and Alpha

At CERN, one of the most unique facilities for antimatter research is the Antimatter Factory, which delivers the world’s only supply of low-energy antiprotons. This resource makes possible a series of precision experiments designed to test whether matter and antimatter obey the same fundamental laws. These studies range from spectroscopy of antihydrogen atoms to direct investigations of how antimatter responds to gravity—questions that are central to addressing the baryon asymmetry problem introduced earlier.

The ALPHA experiment is a key component of this program. In its setup, cold plasmas of positrons and antiprotons are confined within a Penning–Malmberg trap and then carefully combined to form antihydrogen. Since antihydrogen is electrically neutral, it cannot be held in an electrostatic trap; instead, it is confined using a magnetic minimum trap generated by a combination of mirror coils and an octupole field surrounding the Penning electrodes. This allows the atoms to be stored long enough to probe their internal structure with high precision.

Building on this foundation, the ALPHA-g experiment was developed to test the influence of gravity on antihydrogen. Unlike the standard ALPHA configuration, ALPHA-g employs a vertical magnetic trap, which introduces a gravitational potential difference along its axis. By gradually reducing the magnetic field provided by the mirror coils, antihydrogen atoms are released, and their trajectories become biased by the gravitational force. The atoms eventually annihilate on the walls of the apparatus, where a dedicated detector records the positions of these events. From this distribution, information about the gravitational behavior of antihydrogen can be extracted.

## 2.4 Applications of Microwave Injection

### 2.4.1 Microwave Spectroscopy

An extremely important application of injecting microwaves into the ALPHA trap is performing spectroscopy measurements on antihydrogen atoms to determine whether there are differences between the hydrogen and antihydrogen energy levels. ALPHA is a world leader in this field, having recently measured the hyperfine structure of antihydrogen. The essential idea of these experiments is to



use microwaves to resonantly drive atomic transitions [1]. For this reason, accurate knowledge of the electromagnetic field distribution inside the trap is essential for determining the power absorbed by each antihydrogen atom. At present, however, this remains a challenge and constitutes a major source of systematic uncertainty in the experiments, as the field distribution within the trap is not well characterized. The objective of this study is to present a preliminary simulation of the electromagnetic fields in the trap to address this limitation.

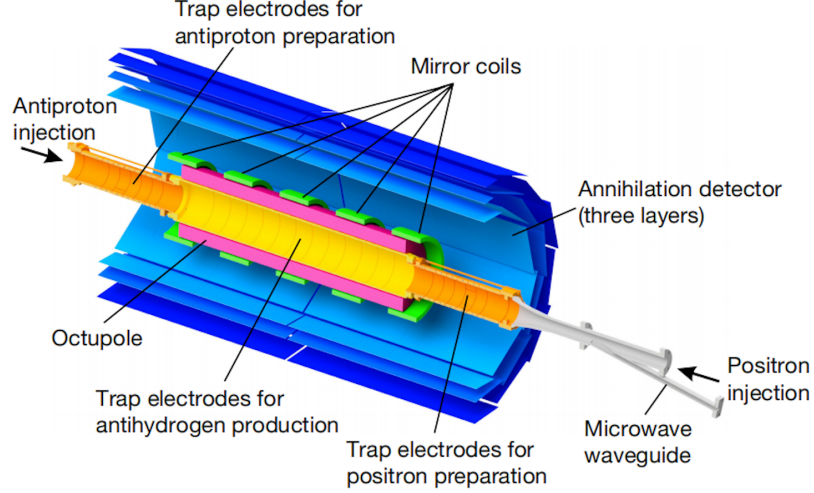


Figure 1: The ALPHA-2 central apparatus. A cut-away schematic of the antihydrogen production and trapping region of ALPHA-2 is shown. For clarity, the vacuum wall and the cryostat for the superconducting magnets are not shown. Antiproton and positron plasmas are prepared on either side of the production region before being mixed to form antihydrogen at the center of the minimum-B trap. All of the components shown are immersed in a uniform, 1-T, axial magnetic field, which is provided by an external solenoid(not illustrated).

#### 2.4.2 ECR Magnetometry

An important parameter in precision experiments with magnetically trapped particles is the magnetic field at each point in space within the trap. One method used to determine the field is called Electron Cyclotron Resonance (ECR) Magnetometry. The basis of the ALPHA ECR technique is the cyclotron motion of charged particles—for example, electrons. The method consists of injecting micro-waves to the trapped charged particle already moving in a circular cyclotron motion (in the x-y plane) due to the confining magnetic field, and creating a driven Lorentz harmonic oscillator system. Then, sweeping through the micro-waves frequencies until a normal mode of oscillation of the system is reached, knowing that at the normal modes of oscillation a heating of the cloud of electrons will be observed. Using the fact that the particles will be moving in a cyclotron motion, the magnetic field may be computed at the cyclotron frequency using the well known equation:

$$B = \frac{2\pi m f_c}{q}, \quad (2)$$

Where B is the magnitude of the magnetic field,  $f_c$  is the cyclotron frequency, m is the mass of the electron and q is the elementary charge. It may be showed that not only heating will be observed at the ECR frequency, but there would also be side peaks at multiples of the bounce frequency (Given that the cyclotron frequency  $\omega_c$  is in the x-y plane, the bounce frequency is  $\omega_z$  corresponding to the frequency in the z axis). For a detailed derivation, please refer to [3].

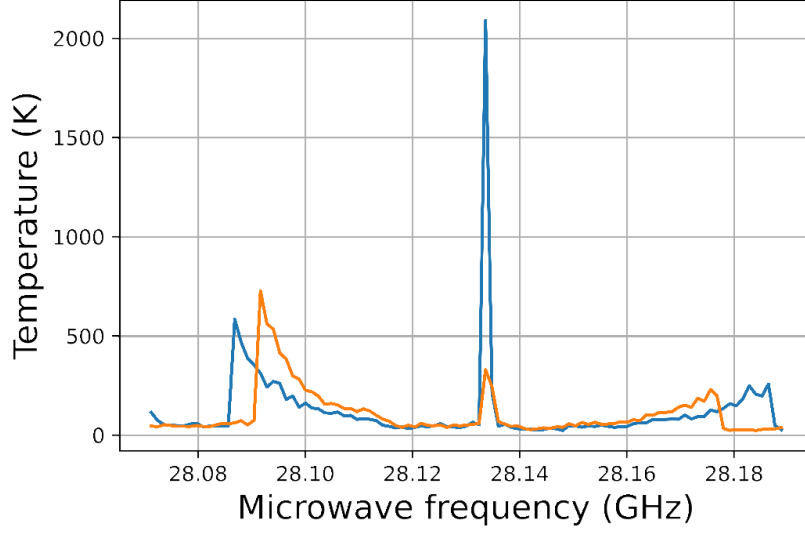


Figure 2: Example ECR spectra with 100 target plasmas each at the same axial location of the ALPHA-g Penning trap with different well depths.

### 3 Alpha-g Hardware Overview

The basic concept for ALPHA-g, is to make a vertical antihydrogen trap with a significant gravitational potential difference at the ends of the magnetic trap. The main components of ALPHA-g are [3]:

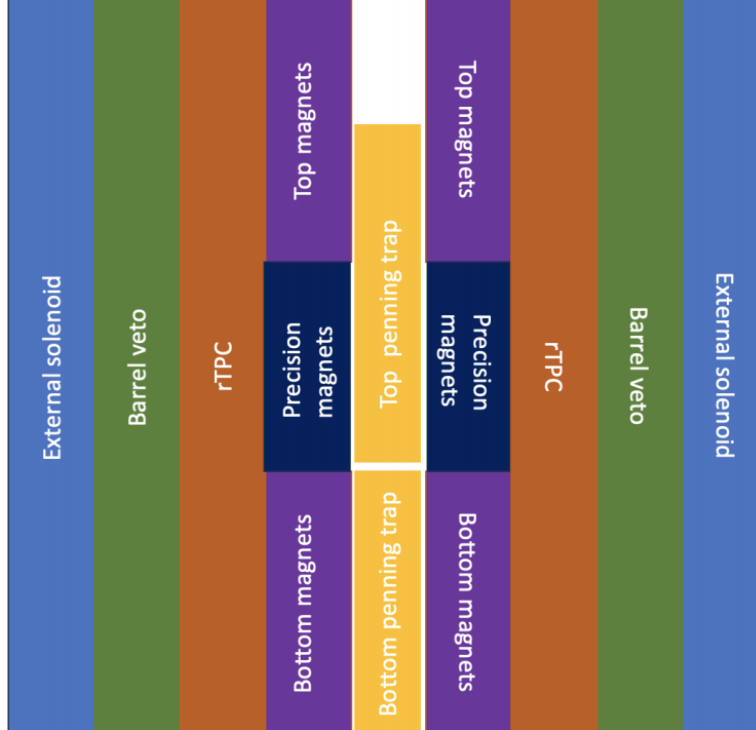


Figure 3: Cartoon diagram showing a cut through of the cylindrical layers of ALPHA-g.

**rTPC:** is the main detector used in reconstructing the annihilations of antiprotons and antihydrogen atoms in ALPHA-g. It is a gas-filled radial time projection chamber using a mixture of carbon dioxide and argon continuously flowing around the anode wires. Charged particles ionize the gas, leaving free electrons, which are accelerated to the anode wires. The current flowing in the anode

wires then induce an image charge on the cathode pads. The timing of these image charges on the cathode pads allow for reconstruction of the track of the annihilation products through the detector.

**Barrel Veto:** As with all particle detection experiments, background rejection is vital, with the main source of background in ALPHA being cosmic rays. The barrel veto is a detector positioned around the rTPC made with 64 trapezoidal scintillator bars with arrays of SiPM at each end. The barrel uses coincidence triggers on multiple bars to distinguish a cosmic signal from an annihilation event (a cosmic ray would only trigger two bars as it passes through the detector in a straight line).

**Top, Bottom and Precision Magnetic Traps:** The magnet system in ALPHA-g consists of a magnetic trap formed by octupoles and short solenoids wound directly onto a steel bore. This bore is connected to the cryostat and sealed, allowing the magnets to be submerged in liquid helium. ALPHA-g employs three magnetic traps—a top trap, a bottom trap, and a precision trap—in order to minimize uncontrolled magnetic fields as much as possible, given the use of superconducting materials.

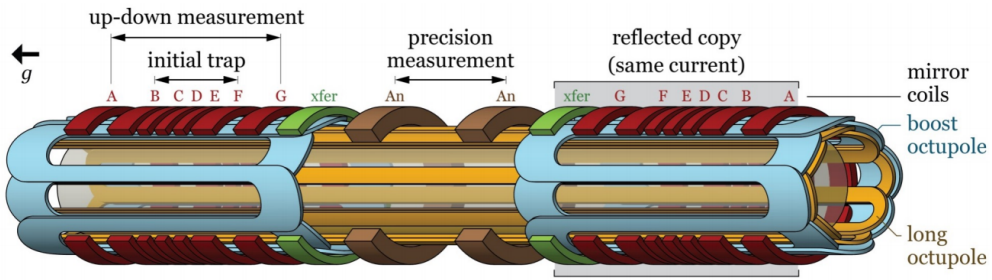


Figure 4: Schematic of the ALPHA-g magnets forming three magnetic minima traps

**Penning Traps :** A Penning trap combines a strong uniform magnetic field with a static quadrupole electric field produced by hyperbolic electrodes for three dimensional confinement of a charged particles motion. Charged particles move according to the Lorentz forced produced by the trapping potential and the Constant magnetic field inside the trap.

The main purpose of the electrodes is to provide for the trapping potential. The thin electrodes are needed since due to magnetic field requirements for magnetic minimum trapping the inner radius of the electrodes in the antihydrogen confinement regions must be as close as possible to the windings of the octopole.

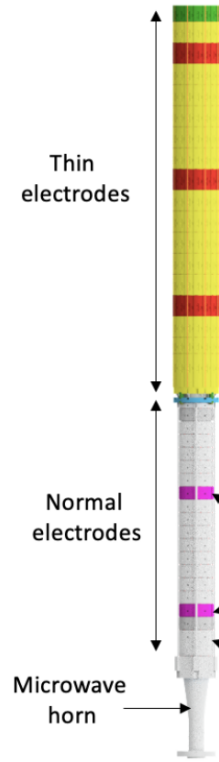


Figure 5: Schematic of the ALPHA-g Penning trap

**Microwave Injection :** The microwave pathway for ALPHA-g begins with a Keysight E8257D synthesizer. This has a frequency range of 100 kHz to 50 GHz and a frequency resolution of 0.01 Hz. For a detailed description of the dimensions please refer to [3].

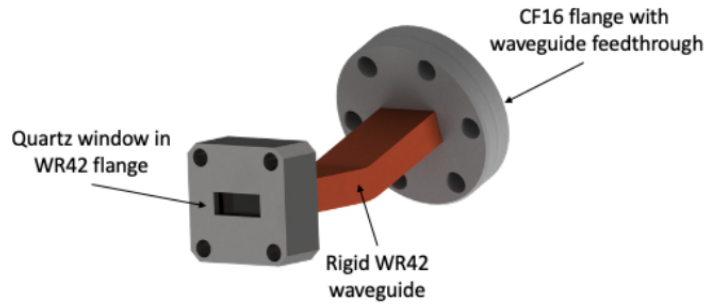


Figure 6: Quartz microwave window assembly to seal ultra high vacuum from air assembly

The micro-wave injection system consists of 3 main sections, starting from a section at room temperature which receives the wave-guide up to the last section at 4 degrees K connected to the penning trap in close to a perfect vacuum conditions.

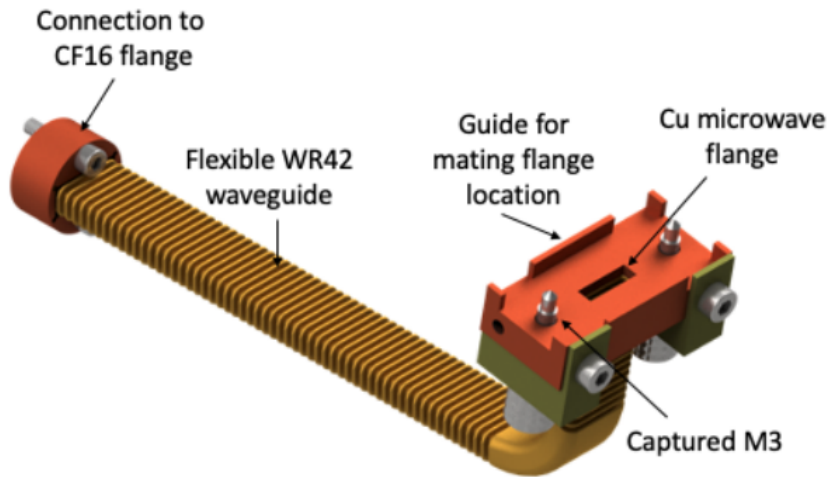


Figure 7: Section 1 of the waveguide path. This flexible guide runs from the microwave window assembly to the titanium heat break which main duty is to decrease the thermal load on the cryostat.

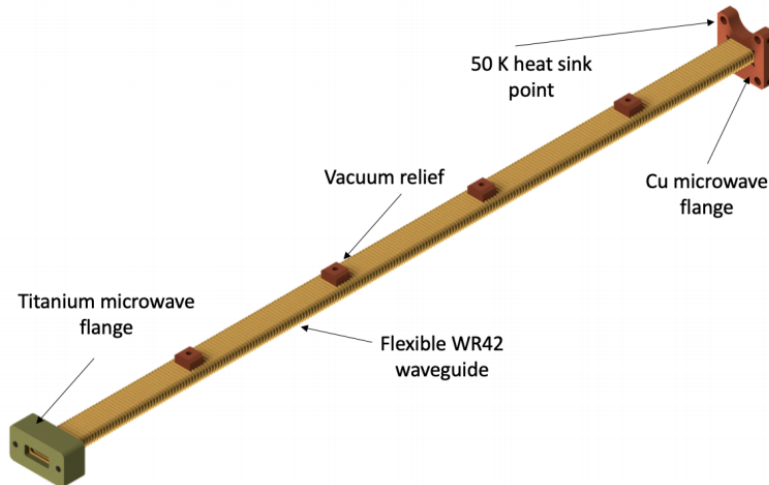


Figure 8: Section 2 of the waveguide path. This section is between room temperature and a 50K stage with a Titanium heat break.

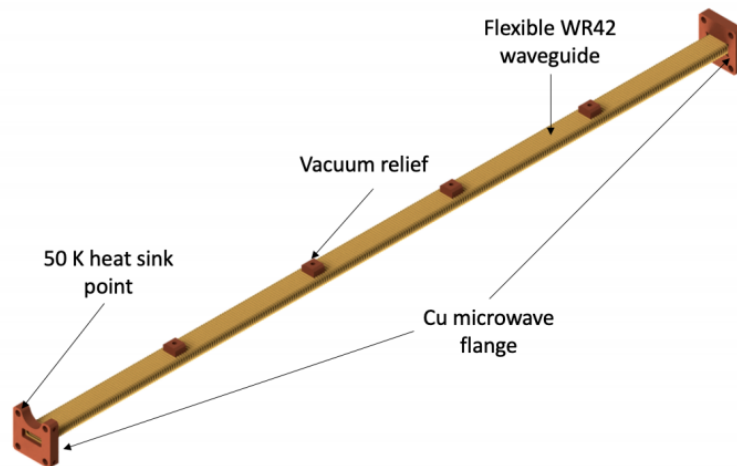


Figure 9: Section 3 of the waveguide path. This section is between a 50K and a 4K stage.

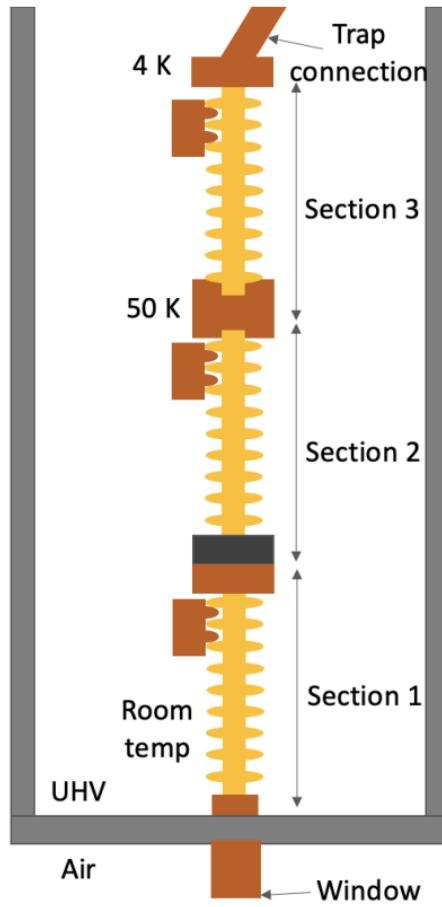


Figure 10: A graph of all 3 sections connected starting from the outside of the trap at room temperature up to the trap connection at 4K.

The purpose of this simulation is to characterize the electromagnetic field distribution beyond the trap connection region, as the field modes in the outer sections of the microwave guides are already well described and can be physically measured prior to integration into the setup.

## 4 Simulations

### 4.1 Software ANSYS HFSS

In this project, we focus on simulating the injection of microwaves into the ALPHA-g Penning trap, taking into account the different geometries and materials involved. For this purpose, we use the software ANSYS HFSS, a 3D electromagnetic (EM) simulation tool for designing and analyzing high-frequency electronic systems.

HFSS solves for the electromagnetic fields within a geometry using the finite element method. It first discretizes the geometry into a series of tetrahedral elements and then solves Maxwell's equations in matrix form on the discretized mesh. To determine convergence of the simulation, HFSS employs a parameter called  $\Delta S$  ("delta S"), which represents the difference in power reflection coefficients within the geometry after each solution step. As the simulation converges to the true solution, the differences in reflection parameters after successive iterations approach zero—that is, the parameters tend toward a constant value.

### 4.2 Base Case 1

As a first step toward the full simulation of the Penning trap, we consider the simplest case: the injection of microwaves into a perfect cylindrical geometry containing only vacuum. For this we will model a vacuum cylinder of 4mm radius and 10 mm height. The convergence parameter  $\Delta S$  was set to 0.02 for a high accuracy solution, and the Fields Plot frequency to 30 GHz.

Designing the basic set-up in HFSS and solving it using the method of finite differences, the following results were obtained:

#### E Field:

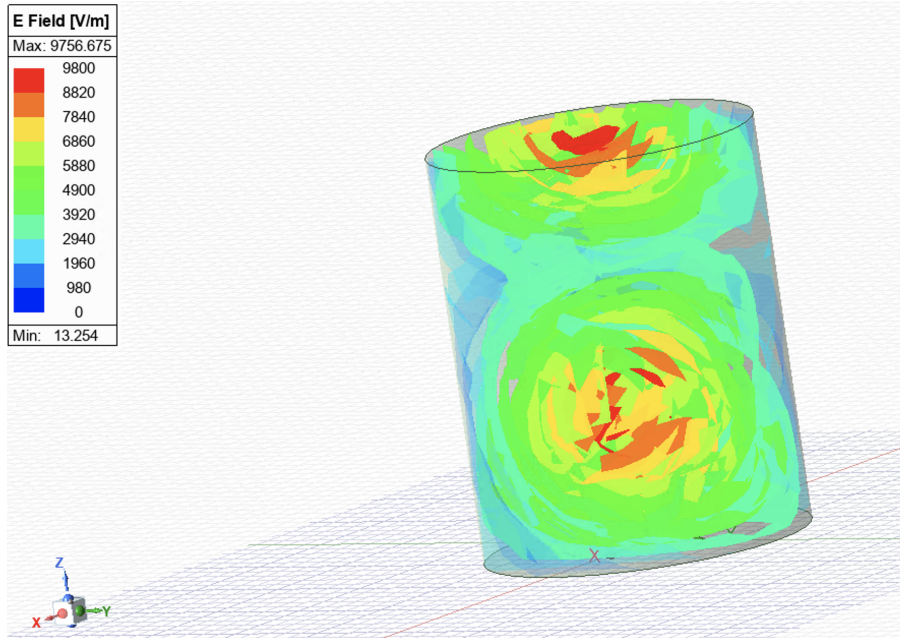


Figure 11: A 3D plot of the electric field distribution within the solution volume for a 30 GHz microwave is shown at its fundamental mode of oscillation. We observe that, due to the absence of metallic reflective surfaces, the spherical waveguides remain unaltered and propagate freely through the geometry. Furthermore, the oscillatory behavior of the injected microwaves can be seen in the form of two independent wave packets traveling throughout the geometry.



## H Field:

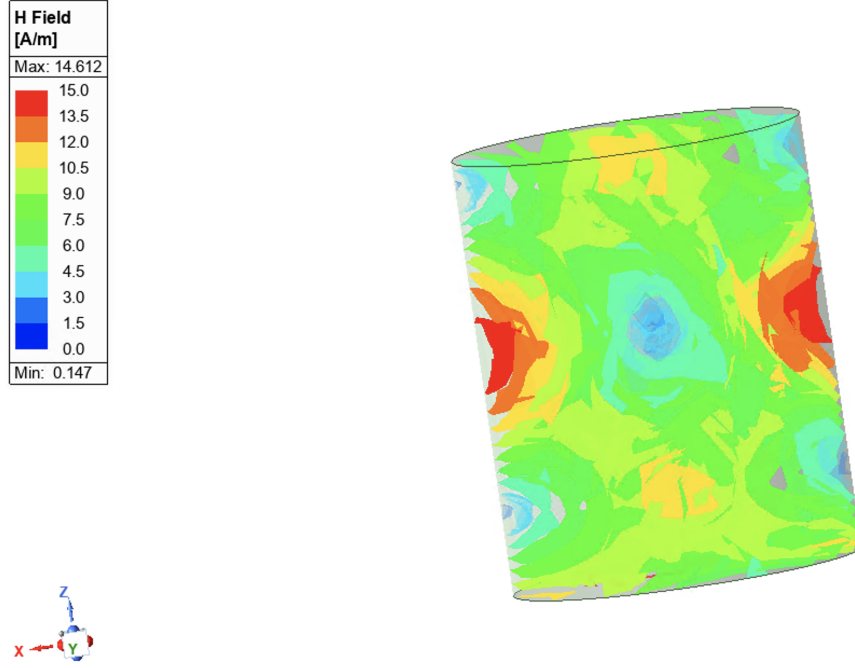


Figure 12: Shown is a 3D plot of the magnetic field distribution within the solution volume at 30 GHz. As expected, the wave-packet behavior characteristic of the injected electromagnetic waves is observed.

## Power Distribution / Poynting Vectors :

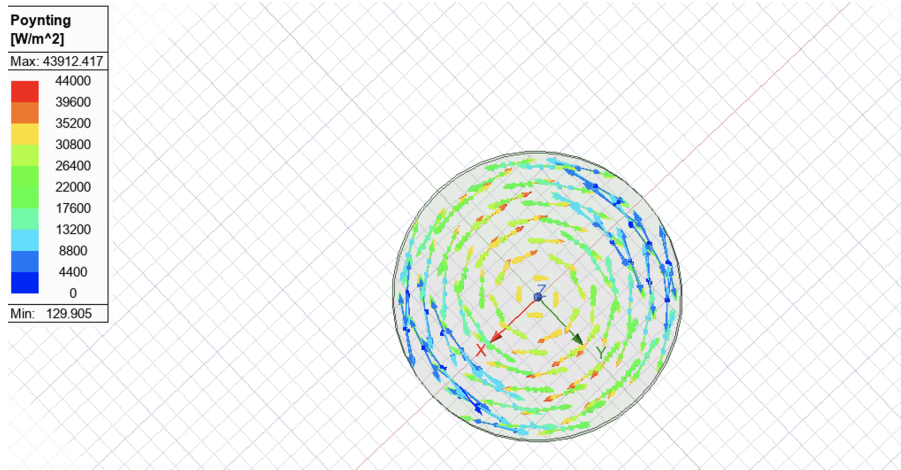


Figure 13: A 2D cross-section of the power distribution within the cylindrical trap. The cylindrical symmetry of the solution is evident, reflecting the idealized geometry. Remembering that the Poynting vector is defined as  $\vec{S} = \frac{1}{\mu_0} \vec{E} \times \vec{B}$  and is pointing in the direction of the wave propagation. It is important to note that the shape of the wave patterns inside the region, as well as the direction of the Poynting field lines, strictly depends on the mode of oscillation excited at the wave port. The patterns presented here correspond specifically to the fundamental mode of oscillation in the cylinder.



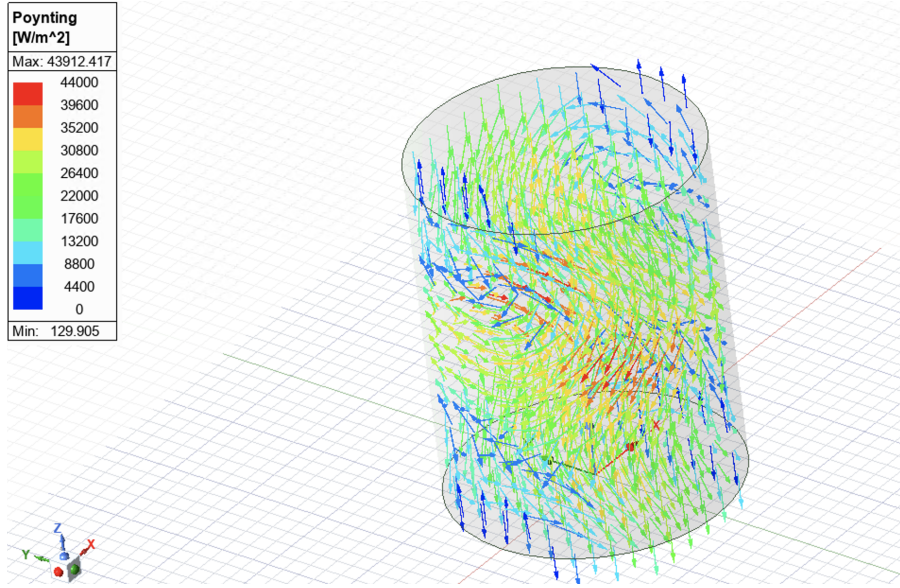


Figure 14: A 3D graph of the power distribution.

### Theoretical Solution

Given that the simulated case consists of a vacuum cylinder, this setup can also be approached theoretically. In vacuum, the electric and magnetic fields satisfy the time-domain wave equations:

$$\nabla^2 \mathbf{E} - \frac{1}{c^2} \frac{\partial^2 \mathbf{E}}{\partial t^2} = 0, \quad (3)$$

$$(4)$$

$$\nabla^2 \mathbf{H} - \frac{1}{c^2} \frac{\partial^2 \mathbf{H}}{\partial t^2} = 0, \quad (5)$$

where  $c$  is the speed of light in vacuum. Now transforming the equation into the frequency domain, assuming time-harmonic fields, we obtain the well known Helmholtz equations:

$$\nabla^2 \mathbf{E}(\mathbf{r}, \omega) + k^2 \mathbf{E}(\mathbf{r}, \omega) = 0, \quad (6)$$

$$\nabla^2 \mathbf{H}(\mathbf{r}, \omega) + k^2 \mathbf{H}(\mathbf{r}, \omega) = 0, \quad (7)$$

where the frequency-dependent wavenumber is

$$k = \frac{\omega}{c}. \quad (8)$$

Now, considering a cylindrical waveguide along  $z$ , with coordinates  $(r, \phi, z)$ . The  $z$ -component of the electric field satisfies

$$\frac{1}{r} \frac{\partial}{\partial r} \left( r \frac{\partial E_z}{\partial r} \right) + \frac{1}{r^2} \frac{\partial^2 E_z}{\partial \phi^2} + \frac{\partial^2 E_z}{\partial z^2} + k^2 E_z = 0. \quad (9)$$

Assume

$$E_z(r, \phi, z, \omega) = R(r)\Phi(\phi)Z(z). \quad (10)$$

Substituting and separating variables gives:

$$\frac{d^2 Z}{dz^2} + \beta^2 Z = 0, \quad (11)$$

$$\frac{d^2 \Phi}{d\phi^2} + m^2 \Phi = 0, \quad (12)$$

$$r^2 \frac{d^2 R}{dr^2} + r \frac{dR}{dr} + ((k^2 - \beta^2)r^2 - m^2)R = 0. \quad (13)$$

Here  $m$  is the azimuthal mode number, and  $\beta$  is the propagation constant, depending on frequency:

$$\beta(\omega) = \sqrt{k^2 - k_c^2} = \sqrt{\frac{\omega^2}{c^2} - k_c^2}, \quad (14)$$

where  $k_c$  is the cutoff wavenumber, determined by the radial Bessel equation and boundary conditions.

The radial equation is a Bessel equation:

$$r^2 \frac{d^2 R}{dr^2} + r \frac{dR}{dr} + (k_c^2 r^2 - m^2) R = 0, \quad (15)$$

with solution

$$R(r) = J_m(k_c r), \quad (16)$$

where  $J_m$  is the Bessel function of order  $m$ .

The complete longitudinal field is

$$E_z(r, \phi, z, \omega) = E_0 J_m(k_c r) e^{im\phi} e^{-i\beta(\omega)z}. \quad (17)$$

(an equivalent method can be used to solve for the H field).

The transverse components can be obtained from  $E_z$  (TM modes) or  $H_z$  (TE modes) .

## S parameters

Another important parameter in the electromagnetic simulations is the power reflection and transmission coefficients, commonly referred to as the S-parameters.

The relationship between incident and reflected waves is given by:

$$\begin{bmatrix} b_1 \\ b_2 \\ \vdots \\ b_N \end{bmatrix} = \begin{bmatrix} S_{11} & S_{12} & \cdots & S_{1N} \\ S_{21} & S_{22} & \cdots & S_{2N} \\ \vdots & \vdots & \ddots & \vdots \\ S_{N1} & S_{N2} & \cdots & S_{NN} \end{bmatrix} \begin{bmatrix} a_1 \\ a_2 \\ \vdots \\ a_N \end{bmatrix}$$

- $a_n$  is the incident (incoming) wave at port  $n$
- $b_m$  is the reflected (outgoing) wave at port  $m$
- $S_{mn}$  is the scattering parameter that represents the fraction of the wave incident at port  $n$  that is transmitted or reflected to port  $m$

This means that  $S_{mn}$  quantifies the response at port  $m$  due to a signal applied at port  $n$ , while all other ports are matched (no reflections).

For this simplified set-up, we will only have 4 S parameters, since there are just two wave-ports in the geometry. A graph below of the S parameters as a function of the incident micro-wave frequency:

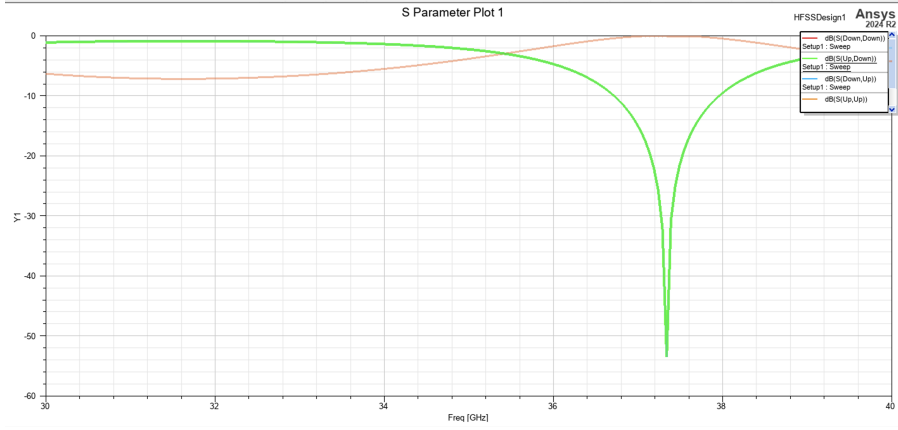


Figure 15: An S-parameter plot as a function of microwave frequency is shown. Owing to the high symmetry of the geometry, the graphs of  $S_{11}$  and  $S_{22}$  are superimposed, as are those of  $S_{12}$  and  $S_{21}$ . This symmetry arises from the fact that, in a perfect cylinder, the amount of power transmitted between opposite ports is identical in both directions, and the same holds for the power reflected at each port.

### 4.3 Base Case 2

For Base Case 2, we introduce additional complexity to the setup by incorporating a material on the cylinder surface, in this case copper. The material properties of copper, such as electric permittivity and magnetic permeability, among others, are taken into account when solving Maxwell's equations within the material and its surroundings. Furthermore, instead of a single cylinder, the model consists of three cylinders arranged coaxially with a gap between them, to approximate the configuration of the actual trap. The specific dimensions of the trap cylinders are not considered at this stage.

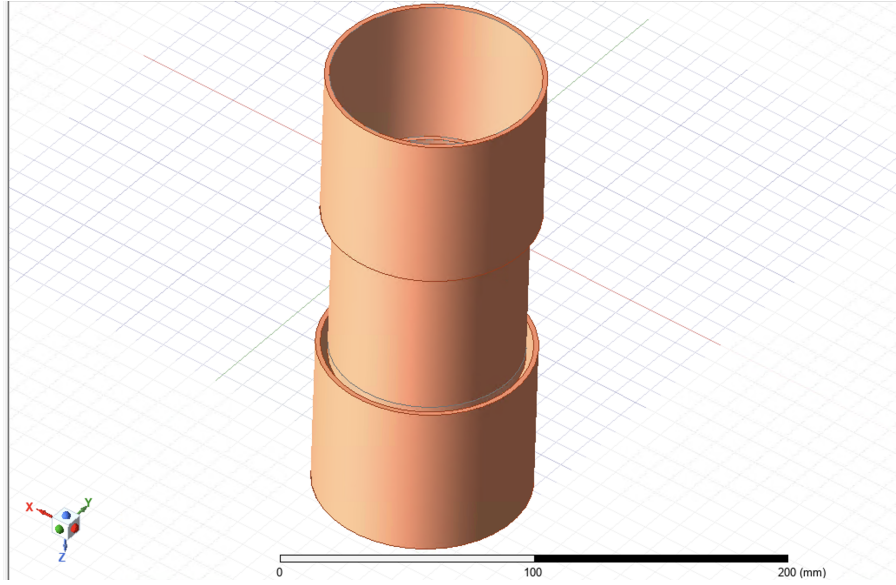


Figure 16: Base Case 2 geometry: composed of three copper cylinders, each with a wall thickness of 2 mm. The central cylinder has an outer radius of 4 cm and a height of 8 cm. The two outer cylinders each have an outer radius of 4.5 cm and a height of 7 cm. The outer cylinders are separated by a distance of 7 cm.

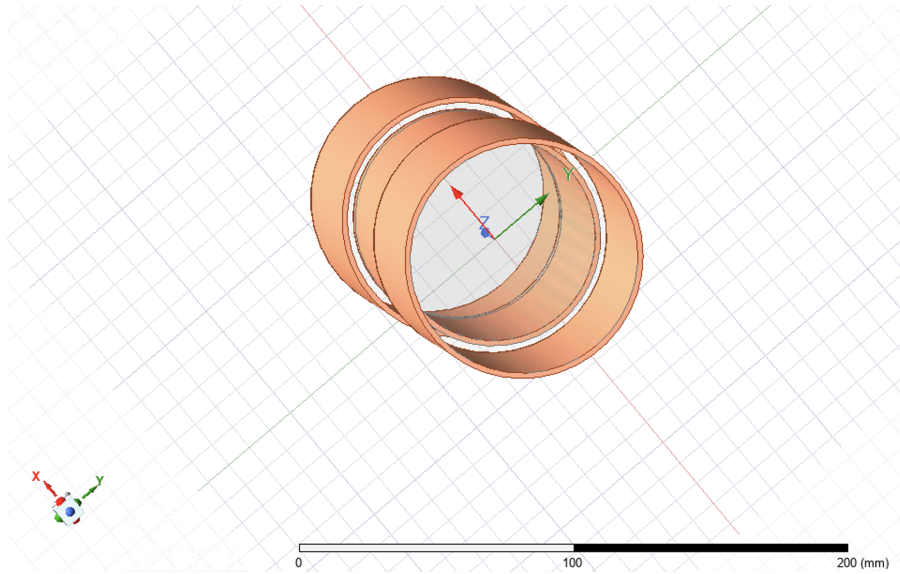


Figure 17: Base case 2 Geometry, X-Y plane view.

## E, H fields and the Poynting vectors

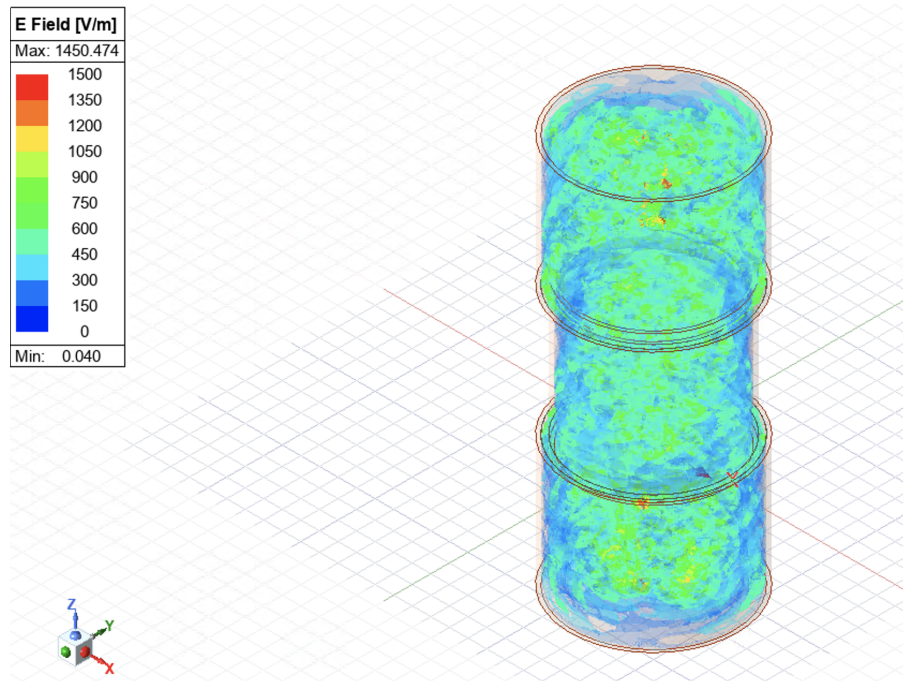


Figure 18: Electric field distribution within the geometry at a frequency of 20 GHz. It can be observed that the well-defined wave-packet structure dissipates in this case due to the presence of reflective geometries, resulting in a more complex wave pattern.

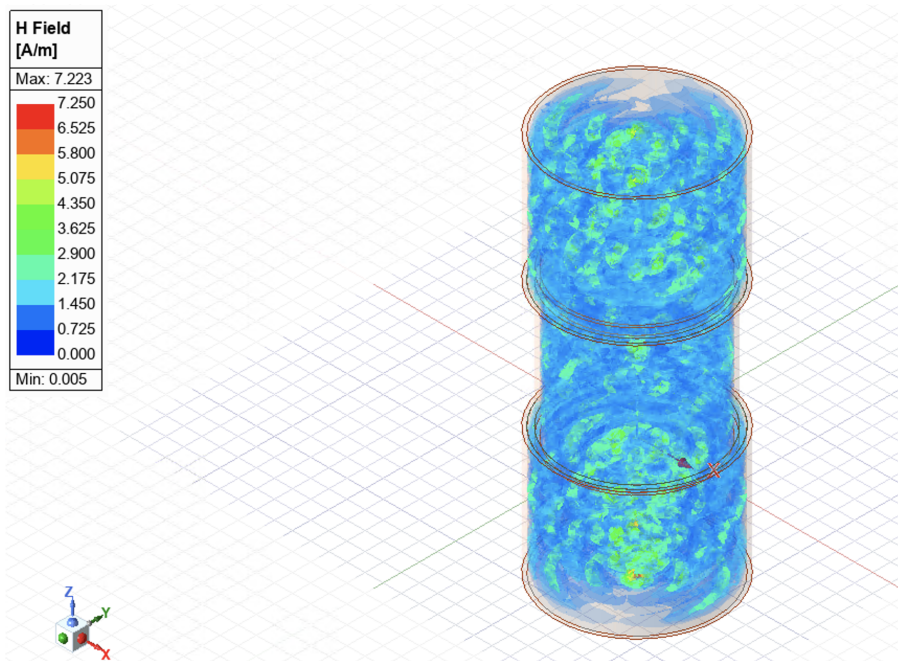


Figure 19: Magnetic field distribution within the geometry at a frequency of 20 GHz. The same phenomenon observed for the electric field occurs here: a complex wave pattern emerges due to the introduction of reflective surfaces and the boundary conditions imposed on the system.



Power Distribution

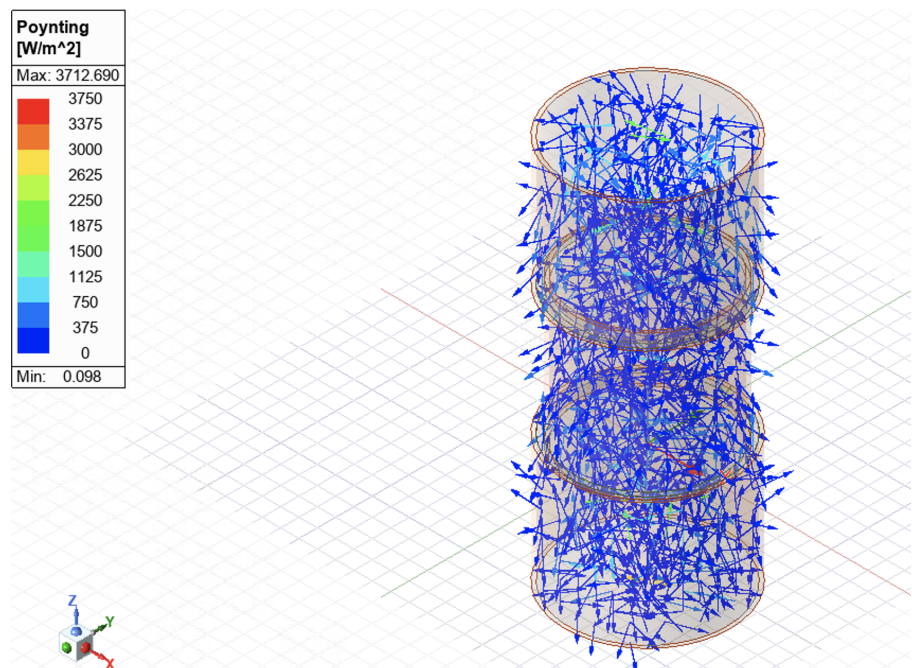


Figure 20: A 3D plot of the power distribution within the cavity. The repeated reflections of the waves inside the cavity are evident, as the Poynting vector is not directed solely toward the opposite end but also indicates energy transfer to the cavity walls throughout the structure. Nevertheless, a net power transfer from one end of the cavity to the other can still be observed.

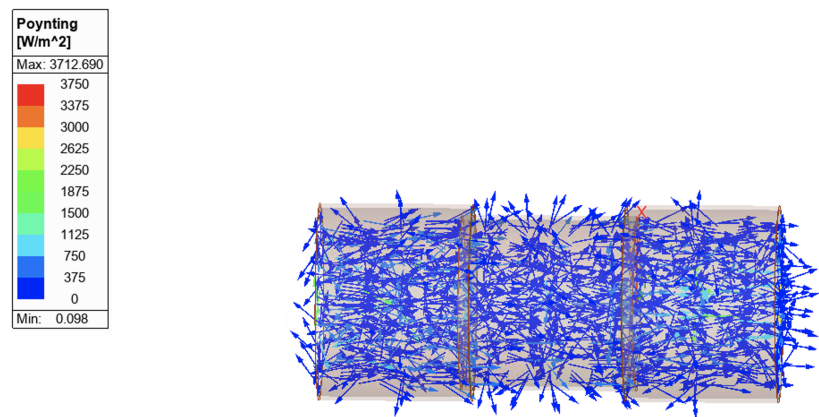


Figure 21: A 3D graph of the power distribution.

## S parameters

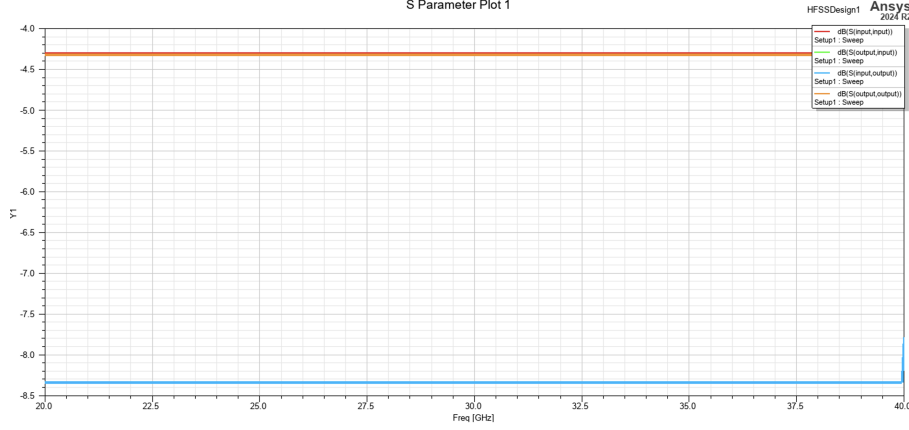


Figure 22: S parameters plot as a function of the microwave frequency. Due to the reflection symmetry of the geometry, the S parameters  $S_{11}$  and  $S_{22}$  overlap, as do  $S_{12}$  and  $S_{21}$ . The primary difference is that the reflection coefficients between opposite ports are now very small, reflecting the increased power loss within the geometry.

### 4.4 Addition of a Microwave Absorbing Material

A potential enhancement to the ALPHA-g trap is the incorporation of a microwave-absorbing material to dissipate the microwave power after its interaction with the trap. This aims to minimize the reflection of microwave signals within the geometry once the power has been deposited, thereby preventing the formation of complex wave patterns inside the trap. To illustrate the effect of such a material on the field distributions, we extend the Base Case 2 simulation by placing a microwave-absorbing material near one of the ports and plotting the resulting power distribution in that region. In this case, the material chosen is CR-110, which is suitable for vacuum conditions and high-frequency operation. The material parameters, including electric permittivity and magnetic permeability at the simulation frequencies, were obtained from previous studies, such as in [4].

The microwave absorber was cylindrical in shape, with a radius of 18 mm and a height of 20 mm. The convergence parameter  $\Delta S$  was set to 0.02 to ensure a high-accuracy solution. The frequency range considered was 20–40 GHz, with 401 frequency points sampled within this interval.

## E, H fields and the Poynting vectors

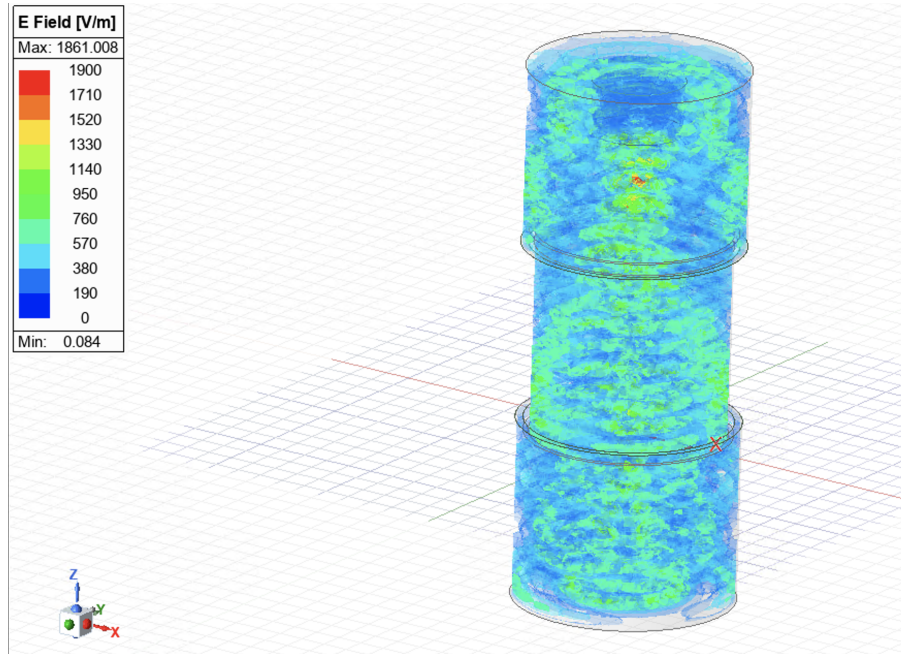


Figure 23: Electric field distribution within the geometry for the frequency of 20 GHz. A high electric field density is observed immediately upstream of the microwave absorber showing the fact that micro-waves are mostly entering the micro-wave absorber.

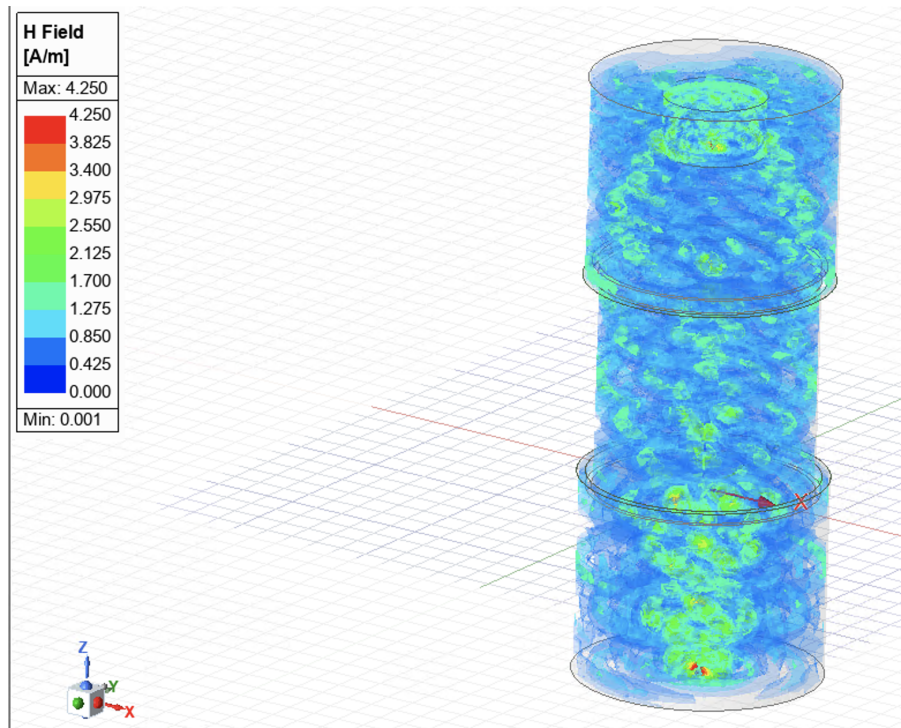


Figure 24: Magnetic field distribution within the geometry at a frequency of 20 GHz. As expected, a high magnetic field density is observed within the microwave absorber.



## Power Distribution

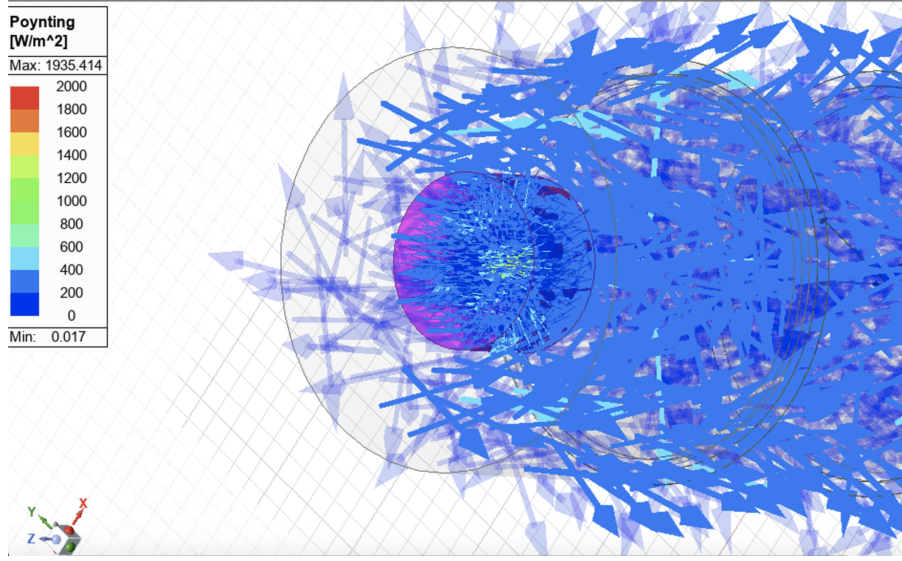


Figure 25: 3D plot of the Poynting vectors surrounding the cylindrical microwave absorber. As expected, a high density of field lines enters the absorber, reflecting its primary function of absorbing microwave power and dissipating it as heat.

## S parameters

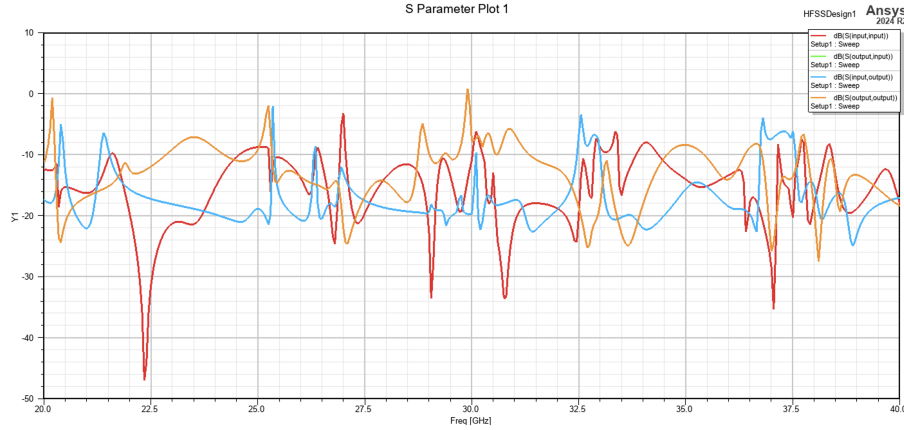


Figure 26: S parameters plot as a function of the microwave frequency. As observed previously,  $S_{11}$  and  $S_{22}$  remain superposed; however, a significant difference now appears between the  $S_{12}$  and  $S_{21}$  parameters due to the asymmetry introduced in the geometry by the micro-wave absorbing material.

## 4.5 Realistic Case

Finally, we consider a case closer to realistic conditions. The simulation examines the electromagnetic fields within a section of the bottom Penning trap, beginning from the microwave injection. The trap is assumed to be primarily constructed of gold. Due to the high complexity of the simulation, the convergence parameter  $\Delta S$  was increased to 0.25 to obtain a solution. The frequency range considered was 29–31 GHz, with 33 frequency points sampled within this range. The realistic dimensions of the trap were included; further details on the trap geometry can be found here[3].

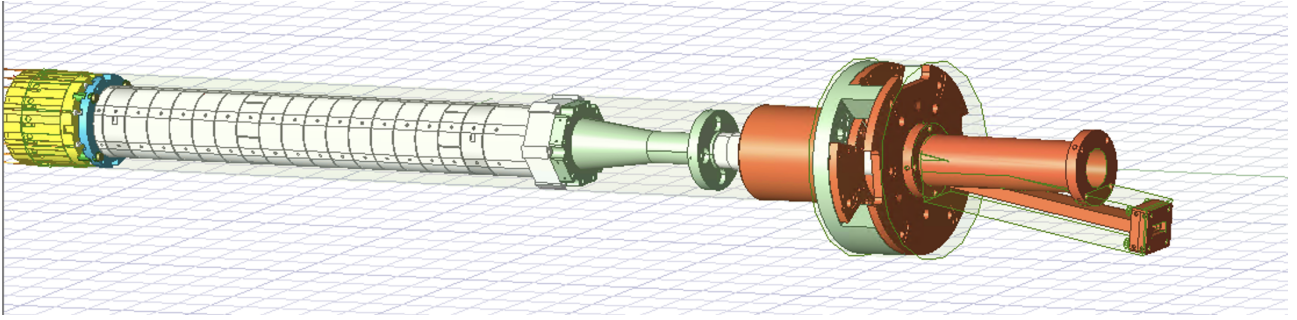


Figure 27: Design in HFSS of the Bottom Penning trap, the microwaves are injected from the microwave guide as explained on the previous sections.

### E field

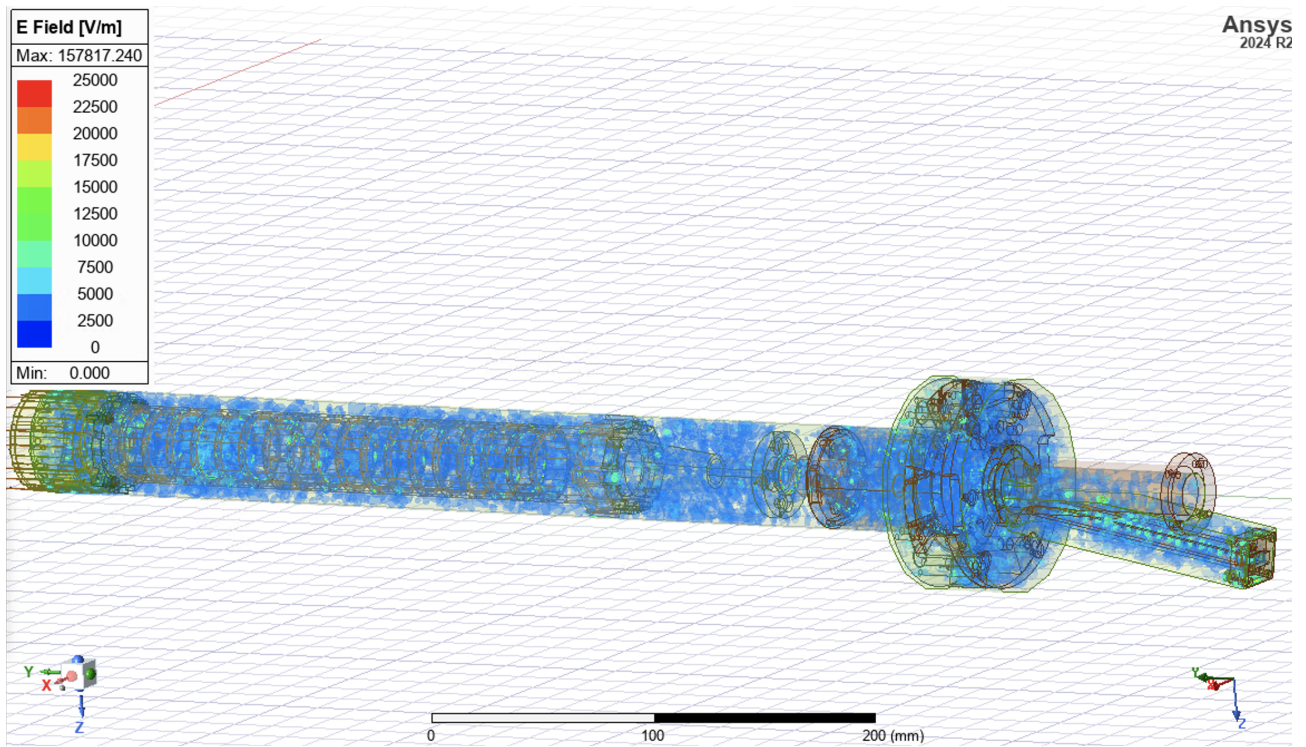


Figure 28: Electric field distribution within the geometry at a frequency of 30 GHz. A high field gradient is observed within the trap, with peak values reaching approximately 160,000 V/m in certain regions. Since most of the trap experiences lower field magnitudes, the field plot has been normalized to display values up to 25,000 V/m. This normalization is the reason why regions outside the trap are visible in the plot, as the scaling allows even the smallest fields to be captured. An interesting phenomenon is also observed: the injection of microwave wave packets into the trap.

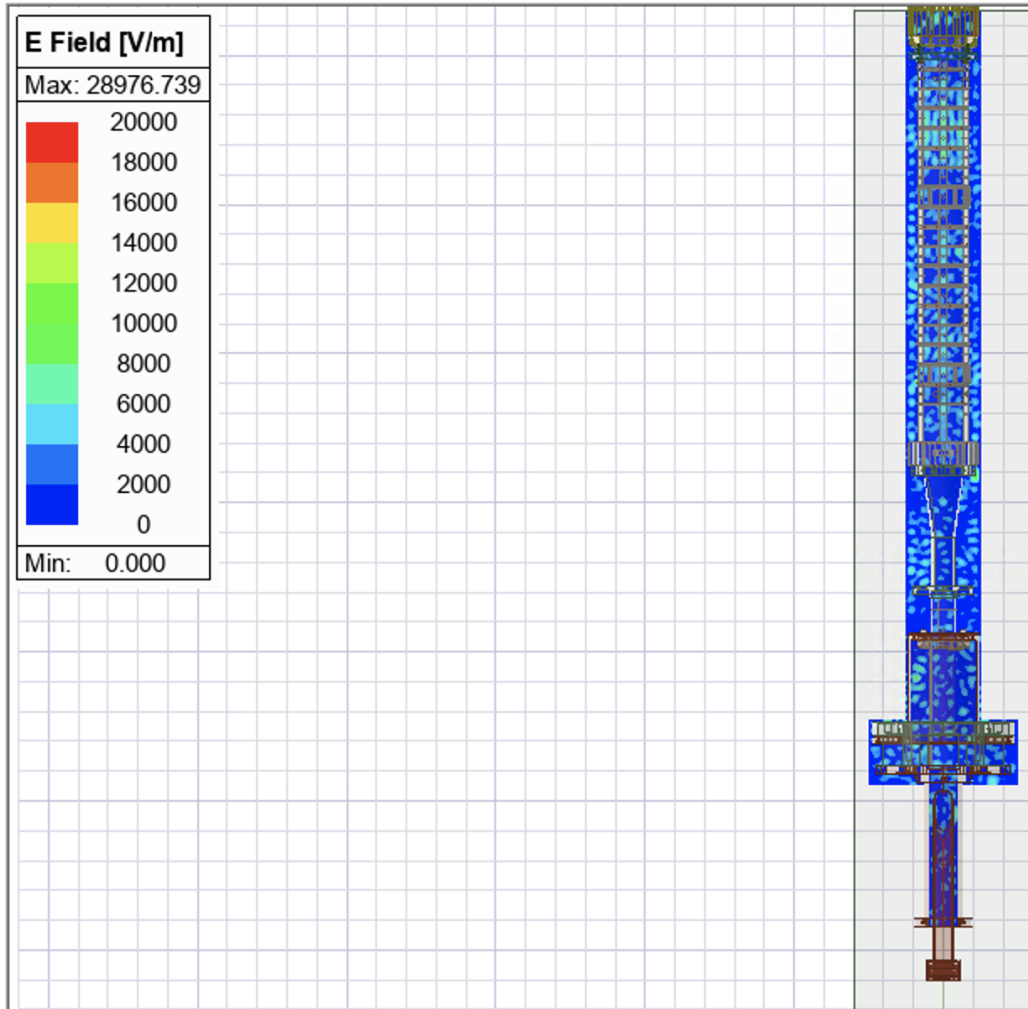


Figure 29: Electric field distribution in an X-Y plane cross-section of the trap.

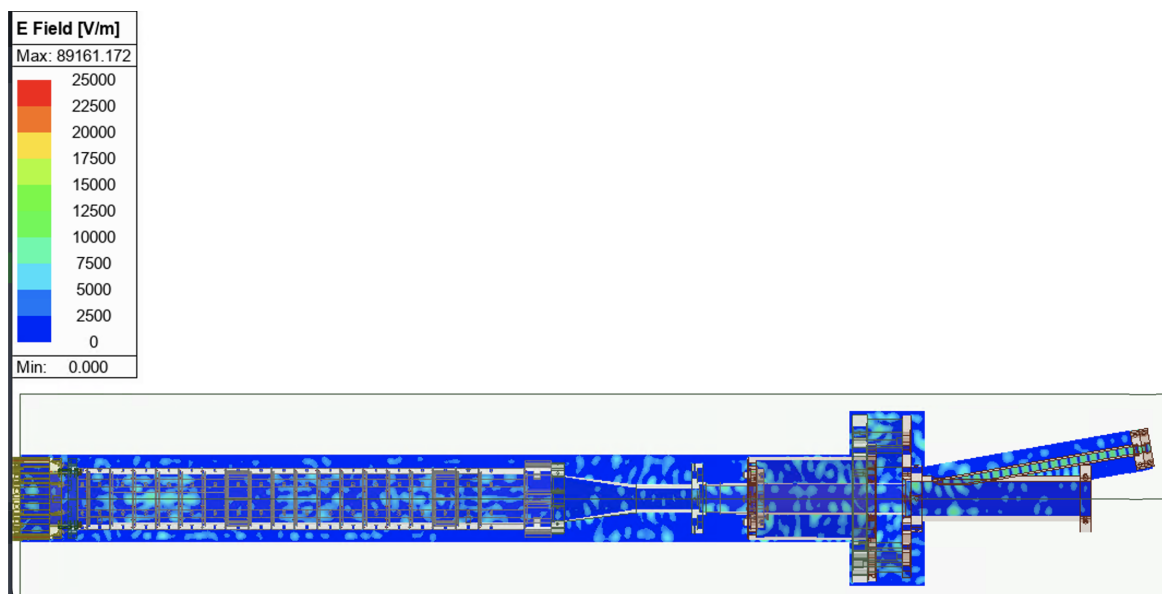


Figure 30: Electric field distribution in a Y-Z plane cross-section of the trap.

## H field

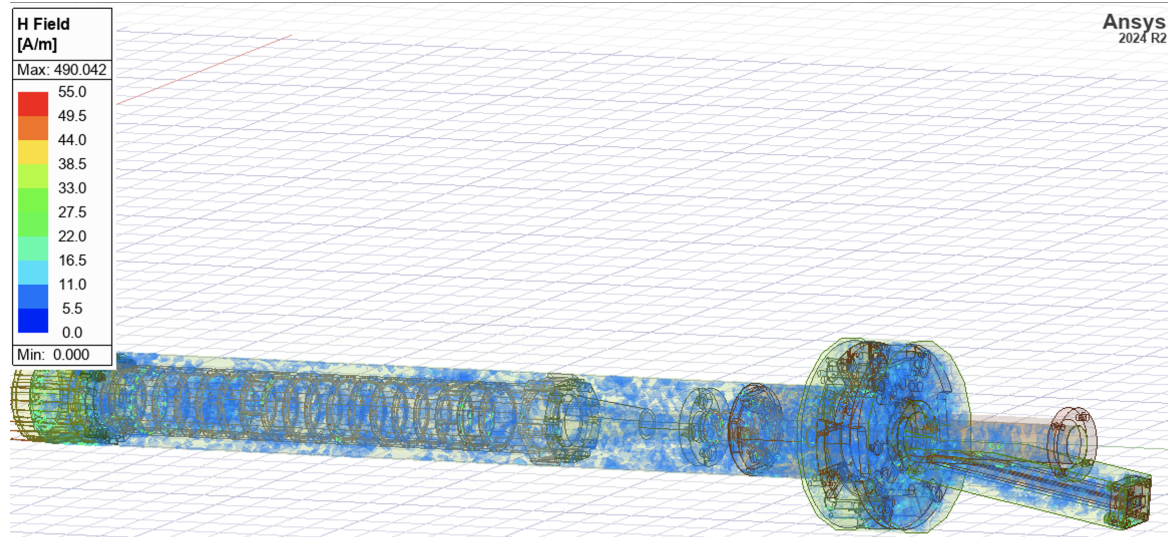


Figure 31: Magnetic field distribution within the geometry at a frequency of 30 GHz. The same phenomena observed in the electric field distribution are also evident here. Due to the high field gradient within the trap, with magnetic fields reaching up to 490 A/m, the plots have been normalized to display values up to 55 A/m. This normalization is the reason why regions with lower magnetic fields are visible outside the main trap region. A high magnetic field is observed at the beginning of the thin electrode zone (yellow area).

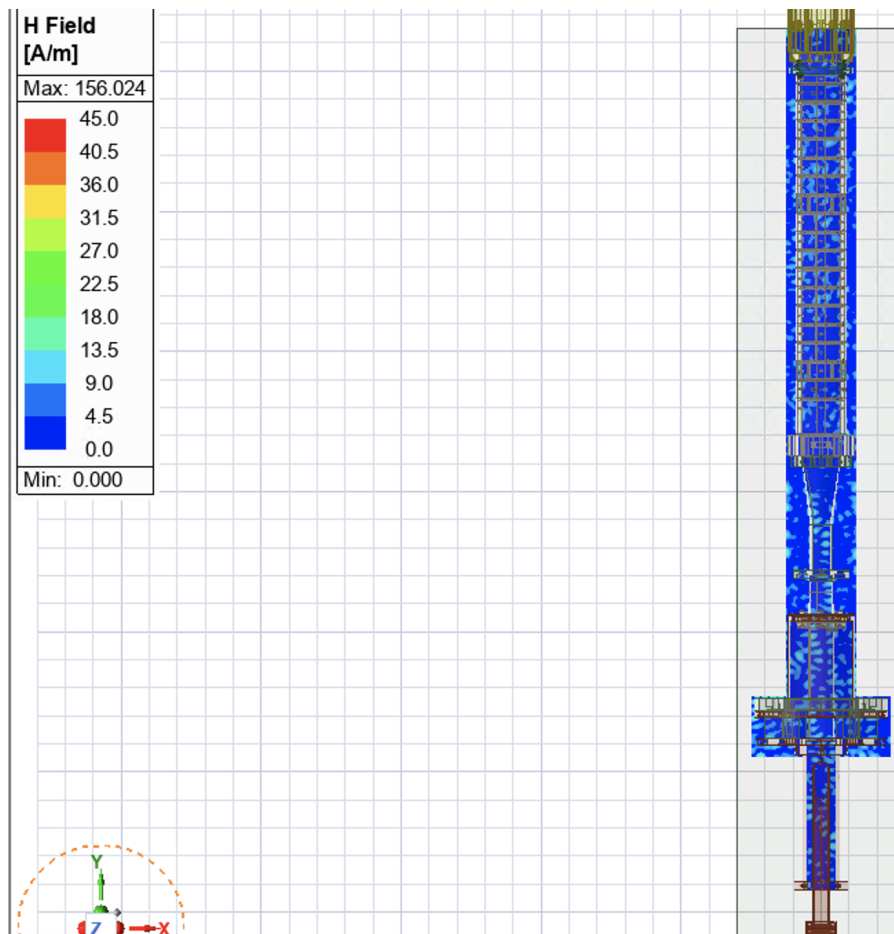


Figure 32: Magnetic field distribution in an X-Y plane cross-section of the trap.



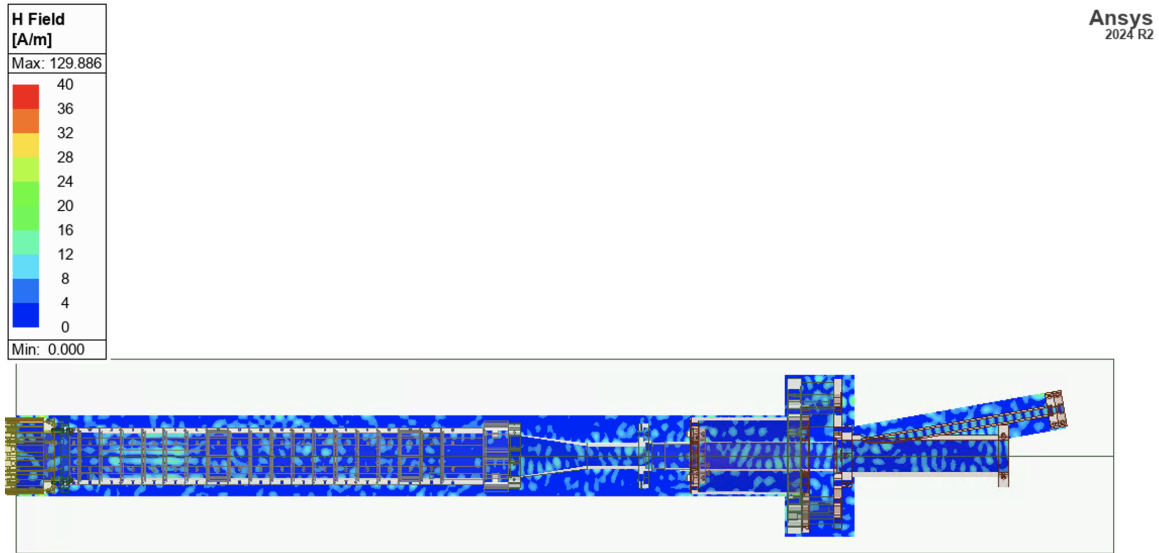


Figure 33: Magnetic field distribution in an Y-Z plane cross-section of the trap.

Analysis of the simulation results reveals a region that receives the highest power within the entire trap, specifically the area shown in the plot below:

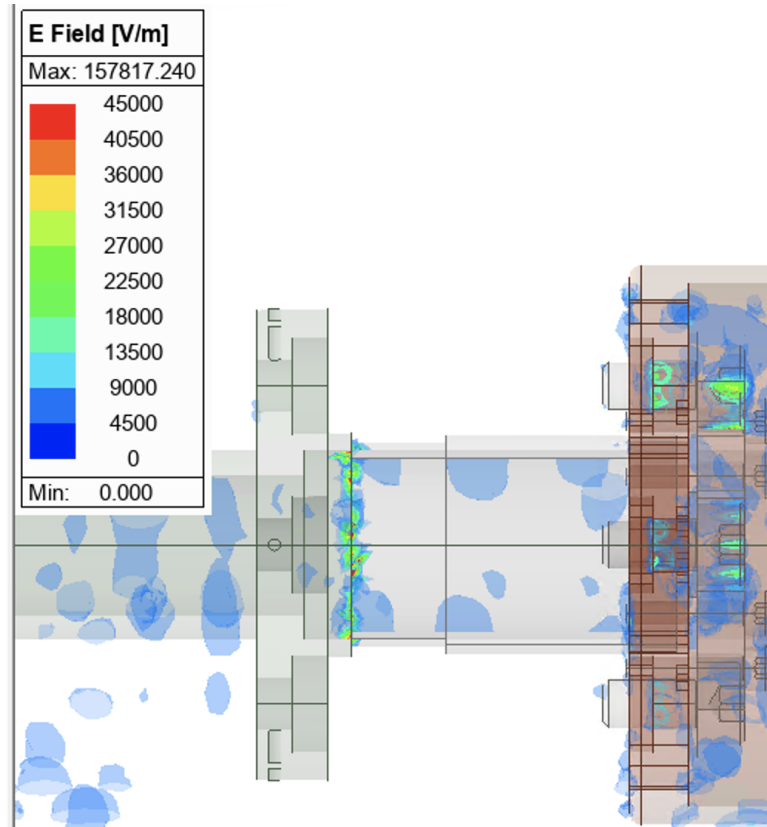


Figure 34: Region receiving the highest density of electric and magnetic fields. Upon reviewing the model, it was noted that the primary reason for the high field density is that these regions are not completely sealed; instead, small gaps between the cylinders allow microwave power to escape. This contrasts with the physical trap, in which the region is fully sealed. More detailed studies are required to achieve a more accurate description of the trap in this region.

## S parameters

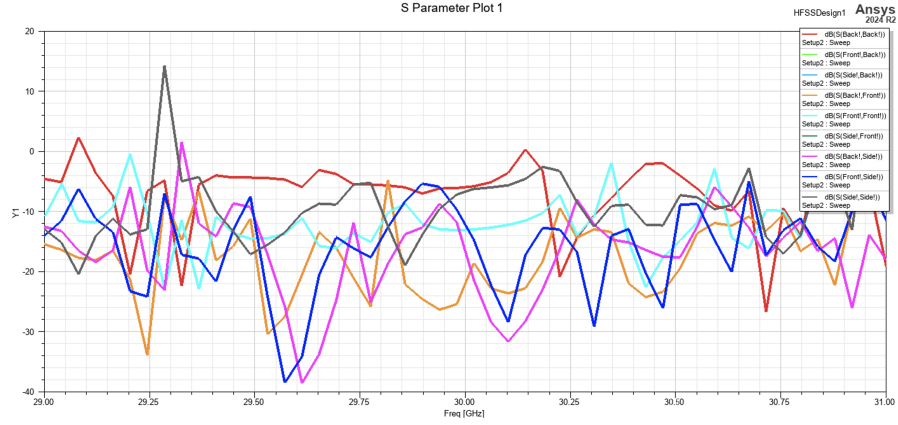


Figure 35: S-parameter plot as a function of microwave frequency within the 29–31 GHz range. The sharp features of the plot are expected, as only 33 frequency points were sampled within this range; these features are anticipated to smooth out in higher-resolution simulations. A large number of critical frequencies can be observed, resulting from the complex geometry of the trap. For this geometry, the microwave guide was defined as the ‘Side’ port, while the adjacent port—typically used for positron injection—was designated as the ‘Front’ port. The ‘Back’ port was defined at the opposite end of the trap, in the region of the thin electrodes (yellow).

## 5 Conclusions

We have developed a preliminary simulation of the electromagnetic fields within the bottom Penning trap of ALPHA-g and have extracted key parameters relevant for spectroscopy and ECR measurements, including the power distribution, the electromagnetic fields, and the S-parameters, in order to evaluate deviations from the simple cylindrical geometry approximation. Due to the high complexity of the simulation, even the realistic model was somewhat simplified—for instance, not all materials were included, and the full trap with all its components was not simulated. More detailed studies are required for a fully accurate description; however, the general behavior of the fields within the trap has been successfully characterized.

## References

- [1] M. Ahmadi, B. X. R. Alves, C. J. Baker, W. Bertsche, E. Butler, A. Capra, C. Carruth, C. L. Cesar, M. Charlton, S. Cohen, et al. Observation of the hyperfine spectrum of antihydrogen. *Nature*, 548:66–69, 2017. doi: 10.1038/nature23446.
- [2] Carl D. Anderson. The positive electron. *Physical Review*, 43(6):491–494, 3 1933. doi: 10.1103/PhysRev.43.491. URL <https://link.aps.org/doi/10.1103/PhysRev.43.491>.
- [3] Adam Michael William Powell. *Magnetic field characterisation for gravitational free fall measurements of antihydrogen in the ALPHA-g experiment*. PhD thesis, University of Calgary, Calgary, Canada, 2024. URL <https://prism.ucalgary.ca/handle/1880/119828>.
- [4] Irena Zivkovic and A. Murk. Characterization of magnetically loaded microwave absorbers. *Progress In Electromagnetics Research B*, 33:277–289, 2011. doi: 10.2528/PIERB11071108.